Sedimentology and geochemistry of thermokarst ponds in discontinuous permafrost, subarctic Quebec, Canada

Frédéric Bouchard,[1,2] Pierre Francus,[1,2] Reinhard Pienitz,[2,3] and Isabelle Laurion[1,2]

[1] Thermokarst (thaw) ponds and lakes are distributed throughout arctic and subarctic regions; however their natural variability and temporal evolution recorded in the bottom sediments are poorly understood. This paper presents a multiproxy study conducted in a subarctic site with many thermokarst ponds near Kuujjuarapik-Whapmagoostui, on the eastern shore of Hudson Bay. Sedimentological, geochemical and chronological analyses have been performed on short sediment cores (10–20 cm) retrieved from limnologically contrasted ponds. Analyses revealed two distinct sedimentary facies, from bottom to top: 1) massive marine silts and clays deposited during postglacial Tyrrell Sea transgression (ca. 8000 to 6000 cal yr BP), subsequently emerged by glacio-isostatic rebound and more recently (ca. 1500 to 400 cal yr BP) affected by permafrost inception and growth; 2) laminated organic-rich lacustrine muds deposited since permafrost thawing and subsidence, i.e., since thermokarst pond inception (the last centuries). Despite displaying strikingly different water colors, the study ponds showed similar long-term developmental patterns regarding their physico-chemical properties (as recorded in the sediments), such as decreasing mineral grain size (from silts to clays), decreasing major chemical element concentrations, increasing organic matter content, and decreasing bottom water oxygen concentrations (from well-oxygenated to anoxic/hypoxic conditions).

1. Introduction

[2] Recent permafrost thawing and erosion in high latitude regions result in the formation of numerous thermokarst (thaw) ponds and lakes. These aquatic ecosystems are widespread throughout arctic and subarctic regions, and can persist from days to thousands of years depending on regional climate, as well as local factors such as geomorphology and hydrology [*Pienitz et al.*, 2008]. Their surroundings may contain vast amounts of organic carbon, formerly trapped in permafrost, that can be partly mineralized to CO_2 and CH_4 in pond and lake water, and then transferred to the atmosphere [*Laurion et al.*, 2010; *Schuur et al.*, 2009; *Tarnocai et al.*, 2009; *Zimov et al.*, 2006]. Thermokarst ponds and lakes can then act as biogeochemical «hotspots» of greenhouse gas (GHG) emissions and may contribute a positive feedback to climate warming by modifying local to regional carbon budgets [*Schuur et al.*, 2008; *Walter et al.*, 2006]. This mechanism may have been partly responsible for the global atmospheric increase in CH_4 during the last deglaciation [*Walter et al.*, 2007].

[3] Permafrost is estimated to affect about 25% of the northern hemisphere, and more than 50% of Canada [*Brown et al.*, 1998]. In the northern part of the Quebec-Labrador peninsula, about one third of the landscape is affected by permafrost and a significant part (in its southern distribution zone) is considered as *warm* permafrost, i.e., near the thawing threshold of frozen ground [*Allard and Seguin*, 1987]. In recent decades, increased air/ground temperatures and snow cover along the eastern shore of Hudson Bay have contributed to the widespread reduction of permafrost-affected areas along a north-south gradient: from less than 25% up north (58°N – [*Vallee and Payette*, 2007]) to more than 80% in southeastern Hudson Bay (56°N – [*Payette et al.*, 2004]). Therefore, thermokarst systems now occupy an increasingly significant surface area of subarctic Quebec. However, their natural variability and temporal evolution, recorded in bottom sediments, has yet to be characterized to fully assess their potential contribution to the regional and global biogeochemical cycles in northern latitudes.

[4] This study is part of a broader research program investigating past, present and future GHG emissions from thermokarst ponds in subarctic Quebec [*Breton et al.*, 2009; *Laurion et al.*, 2010; *Watanabe et al.*, 2011]. The overall objectives of this study were 1) to describe the physico-chemical properties of the sediments (i.e., sedimentary

[1]Institut national de la recherche scientifique, Centre–Eau Terre Environnement, Quebec, Quebec, Canada.
[2]Centre d'études nordiques, Université Laval, Quebec, Quebec, Canada.
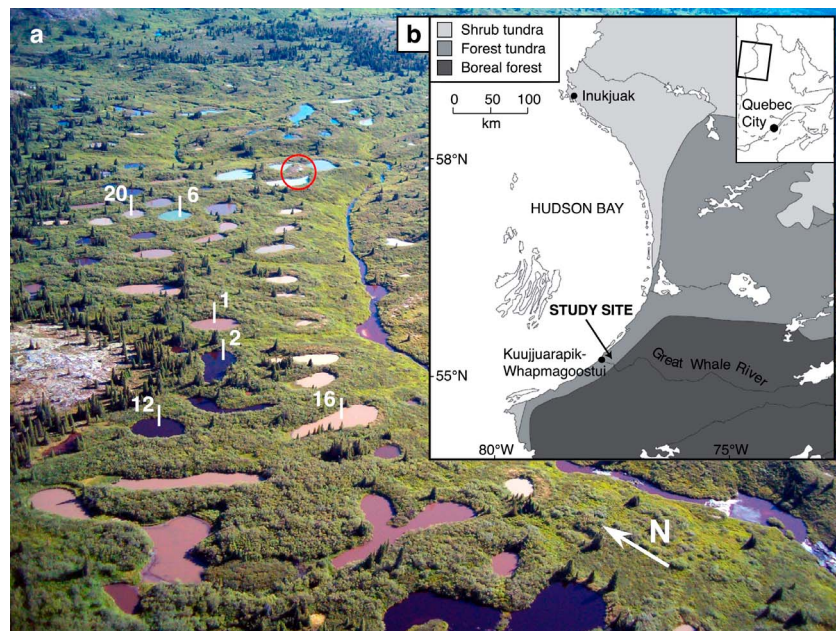[3]Département de Géographie, Université Laval, Quebec, Quebec, Canada.

Figure 1. Location of the study site. (a) Oblique aerial photograph showing sampled ponds (numbers as in the text). The red circle shows the location of the only permafrost mound (lithalsa) still present in the field. (b) Regional map showing vegetation zones in subarctic Quebec. The study site (55°20′ N; 77°30 W) is located near Kuujjuarapik-Whapmagoostui, along the Great Whale River.

facies) in limnologically contrasted ponds, 2) to identify the main processes controlling sediment erosion, transport and deposition in the past and 3) to evaluate the temporal evolution of the ponds in the context of paleoenvironmental changes in their vicinity. In a wider perspective, it provides the lithostratigraphic background on which present-day conditions (e.g., geomorphology, biology, optical properties) can be interpreted. This paper presents the results obtained from six ponds covering a wide range of contrasting limnological properties. Physical and chemical properties of the sediments were examined using a multi-proxy approach, combining «classic» techniques (e.g., grain size analysis, thin sections, loss-on-ignition) and more innovative methods (X-ray micro-fluorescence and micro-radiography). In addition, short-term and long-term chronologies of the sediments were established by radio-isotopic dating techniques (^{14}C, ^{210}Pb and ^{137}Cs). To our knowledge, this is the first documented sedimentological study concerning small thermokarst ponds derived from the thawing of palsas/lithalsas at northern latitudes, contributing to a growing literature on thermokarst pond evolution.

2. Study Area

[5] The study site (55°20′ N; 77°30′ W; 105 m a.s.l.) is located ~20 km inland from the eastern shore of Hudson Bay, near the hamlet of Kuujjuarapik-Whapmagoostui in subarctic Quebec (Figure 1). The granitic/gneissic bedrocks in the area were strongly eroded by Pleistocene glaciations, the last one (Wisconsinan) ending in the area around 8000 years ago when the Laurentide Ice Sheet (LIS) retreated northward and eastward [*Dyke and Prest*, 1987]. Final break-up of the LIS was accompanied by the rapid final outburst of proglacial lake Agassiz-Ojibway and the formation of the Late

Glacial Sakami moraine [*Barber et al.*, 1999; *Hillaire-Marcel et al.*, 1981; *Lajeunesse and St-Onge*, 2008; *Veillette*, 1994]. This deglaciation was followed by the postglacial Tyrell Sea transgression (~7900 cal yr BP), which submerged the landscape up to present-day elevations of 250–300 m and left thick deposits of marine silty clays and littoral sands in topographic depressions [*Hillaire-Marcel*, 1976; *Saulnier-Talbot and Pienitz*, 2001]. Post-glacial emergence of the area occurred at about 6000 cal yr BP and isostatic rebound is now estimated at 1.1 m per century, one of the fastest in the world [*Allard and Tremblay*, 1983].

[6] The prevailing climate is subarctic. Mean annual air temperature at the Kuujjuarapik weather station (55°17′ N; 77°45′ W; 10 m a.s.l.) is −4.4°C, ranging from monthly means of −23.4°C in January to 11.4°C in August [*Environment Canada*, 2010]. Annual freezing index (sum of degree-days below zero) is more than twice the thawing index (sum of degree-days above zero), i.e., 2890 versus 1310 respectively. Annual precipitation is about 650 mm, with more than 35% falling as snow. Snow starts to accumulate on the ground in September–October, reaches a maximum depth (~40 cm) in March, and disappears at the end of May. The snow distribution pattern is strongly controlled by winter (December to March) wind direction, mainly easterly although maximum winter gusts come from west to southeast. The study area lies at the southern edge of the discontinuous and scattered permafrost zone, where less than 50% of the land surface (mainly exposed hills and peatlands) is affected by permafrost [*Allard and Seguin*, 1987].

[7] The study site is a small peatland formerly affected by permafrost, now in an advanced state of degradation. The thawing of permafrost mounds (mainly mineral palsas or lithalsas) has resulted in the formation of several thermo-

Table 1. Limnological Properties and Core Lengths for Sampled Ponds, Including Dissolved Organic Carbon (DOC), Total Suspended Solids (TSS), Secchi Depths (Secchi), and Upper Sediment (Facies) Thickness (Upper Sed)

Pond	Depth (m)	Color	pH	DOC (mg L^{-1})	TSS (mg L^{-1})	Secchi (m)	Core	Length (m)	Upper Sed (cm)
K1	2.25	brown	6.63	7.62	6.26	0.53	K1P2	0.14	4.5
K2	3.00	black	6.31	5.91	2.79	1.40	K2P1	0.17	2.0
							K2P2	0.17	2.0
K6	3.50	blue-green	6.26	3.80	3.75	0.86	K6P1	0.20	2.5
							K6P2	0.10	3.0
K12	2.70	black	6.28	6.95	2.52	1.21	K12P2	0.15	2.5
K16	2.30	beige	7.24	8.74	24.30	0.22	K16P1	0.19	1.0
							K16P2	0.18	1.5
K20	2.65	beige	6.27	7.71	22.16	0.30	K20P1	0.16	2.0

karst ponds (Figure 1). These ponds are generally round (10–30 m diameter) and shallow (1–3.5 m depth). In most cases they are surrounded by a 1–2 m high peripheral ridge covered by dense shrub and tree vegetation. Based on sediment sampling of these peripheral ridges (to be presented in a forthcoming paper) and on former studies in the area [*Arlen-Pouliot and Bhiry*, 2005; *Bhiry and Robert*, 2006; *Calmels et al.*, 2008], the marine sediments *between* and *underneath* the ponds are assumed to be permafrost-free. In fact, only one lithalsa, severely affected by thawing, is still visible on the site (Figure 1).

[8] The studied thermokarst ponds have strikingly differing limnological properties (Table 1), including dissolved organic carbon (DOC), total suspended solids (TSS) and color (detailed limnological description of these ponds are given by *Breton et al.* [2009], *Laurion et al.* [2010] and *Watanabe et al.* [2011]). Most of them are highly humic and nutrient-rich ecosystems where dissolved organic matter (DOM) has a dominant allochthonous source derived from thawing permafrost soils [*Breton et al.*, 2009]. In spite of shallow water depths, these ponds are strongly stratified for most part of the year, with a hypoxic to anoxic hypolimnion, and are considered heterotrophic systems with largely supersaturated concentrations of CO_2 and CH_4 [*Laurion et al.*, 2010]. The vegetation cover in the study area is typical of the forest-tundra zone in subarctic Quebec. Sparse trees and shrubs (e.g., *Picea mariana*, *P. glauca*, *Larix laricina, Ledum groenlandicum, Betula glandulosa*) are abundant on top of peripheral ridges, whereas poorly drained soils between the ponds are mostly occupied by thick shrubs (*Salix* sp., *Alnus crispa*, *Myrica gale*), mosses (*Sphagnum* spp.), and herbaceous plants (e.g., *Carex aquatilis*). The ponds are located in the upper section of a small valley that gently slopes to the south toward the Kwakwatanikapistikw River (local Cree name), a tributary of the Great Whale River. Although the landscape is relatively flat, a slight topographic and hydrologic gradient extend from the west (adjacent granitic/gneiss rocky hills) to the east (steeply embedded creek).

3. Materials and Methods

3.1. Field Sampling

[9] In July 2007, short sediment cores (total length = 10 to 20 cm) were taken in 6 thermokarst ponds covering a wide range of limnological properties (Table 1). For each sampled pond, the deepest part was located with a portable sonar and at least two cores were collected with a 7-cm diameter

handheld percussion corer (Aquatic Research Instruments). Sediment core lengths were restricted by the occurrence of a very sticky and compact clay unit underlying the recent lacustrine sediments (organic mud or gyttja). In order to prevent the mixing of the water-sediment interface, water from above the sediment surface was removed from the core tubes immediately after retrieval by drilling 2 or 3 small holes through the coring tubes just above the water-sediment interface. The cores were then stored vertically at non-freezing conditions for at least 48 h, allowing the upper sediments to slowly consolidate by dewatering. Cores were finally sealed with floral foam blocks to minimize potential disturbances during subsequent transport and brought back to the laboratory, where they were kept in the dark at 4°C.

3.2. Multiproxy Sediment Core Analysis

[10] Sediment cores were cut along their longitudinal axis with a rotating saw and a thin stainless steel wire, and split in two halves. Before each subsequent analysis, disturbed or altered sediment was removed from split core faces by carefully running a stainless steel knife blade parallel to the sediment structures (laminations). Split cores were visually described and photographed with a 500 dpi resolution digital camera. If present, wood fragments or organic debris were collected in glass bottles for subsequent ^{14}C dating (see next section). From that moment on, split cores were covered with a plastic film and kept in the dark (at 4°C) to minimize surface oxidation and desiccation.

[11] High resolution, non-destructive X-radiography and X-ray fluorescence (XRF) analyses were performed with an Itrax Core Scanner [*Croudace et al.*, 2006]. Itrax system uses a flat and intense micro-X-ray beam that incrementally irradiates the advancing sample to obtain 1) gray scale (16-bit) micro-radiographs, and 2) relative concentration of chemical elements by μ-XRF (from Al to U). X-radiographs are 14 mm wide with a pixel size of 0.1 mm, and the resulting gray scale values mainly reflect the sediment bulk density (with darker and lighter grays representing higher and lower density, respectively). XRF measurements have been performed at a downcore resolution of 0.2 mm with an exposure time of 10 s. Final results, given in peak area integrals for each element (dispersive energy spectrum), were normalized by the total counts per second of each spectrum (kcps) to take into account the nature of the sediment matrix. These results were also expressed as ratios to a detrital phase element (K, Rb or Ti) in order to detect supplementary geochemical inputs different from the background concentration of detritic elements [*Rothwell et al.*, 2006].

[12] Longitudinal sediment sub-samples were collected for thin section preparation. Overlapping (~1 cm) thin-walled aluminum trays (18 cm-long × 2 cm-wide × 0.7 cm-deep) were inserted in the surface of the split cores [*Lamoureux*, 1994] and retrieved with a cheese-cutter-style device [*Francus and Asikainen*, 2001]. Sub-samples were then quickly frozen in liquid nitrogen, freeze-dried and impregnated in a low-viscosity epoxy resin [*Lotter and Lemcke*, 1999]. Impregnated blocks were cut with a diamond trim saw and sent to a commercial shop for final thin section preparation. Thin sections were observed and photographed (with 2.5 × and 10 × magnification) using a petrographic microscope equipped with a camera device (5.0-megapixel CCD capturing images of 2560 × 1920 pixels).

[13] Supplementary discrete sub-sampling of the cores was done at 0.25 to 0.5 cm intervals for the surface sediments (top 4–5 cm) and at 0.5 to 1 cm intervals for the bottom sediments. Sub-samples were freeze-dried for at least 48 h, depending on water content. About 0.5 g of dry sediment was extracted to perform loss-on-ignition (LOI) measurements by a subsequent combustion at 550°C for 4 h [*Heiri et al.*, 2001]. Organic content (LOI) and wet/dry sediment mass measurements were used to determine the sediment dry bulk density. Another 0.5 g of sediment was extracted and digested with hydrogen peroxide (H_2O_2 30%) and sodium hydroxide (NaOH 1M) to remove organic matter and biogenic silica, respectively. Samples were then added to a sodium hexametaphosphate solution (10%) and finally sieved (<2 mm) and disaggregated in an ultrasonic bath (at least 90 s) to perform grain size analysis. Measurements were done with a Beckman-Coulter LS-13320 (0.4 to 2000 μm range) and the results of 2 or sometimes 3 runs were averaged. Data were arranged as x (grain size), y (depth) and z (volume %) axis, to be visualized as 3D surface plots [*Beierle et al.*, 2002]. Standard statistical parameters (e.g., mean, median, mode, sorting, skewness and kurtosis) were calculated with the GRADISTAT 4.0 software [*Blott and Pye*, 2001] using the mathematical method of moments [*Krumbein and Pettijohn*, 1938]. The remaining sediment was used to perform ^{210}Pb and ^{137}Cs dating.

3.3. Chronology

[14] Bulk sediment samples, and when present, fossil organic/wood fragments were carefully extracted and dried in glass bottles at 105°C [*Björck and Wohlfarth*, 2001]. Samples were pre-treated (HCl-NaOH-HCl) and combusted to CO_2 at the Radiocarbon Dating Laboratory (Laval University, Quebec City QC, Canada) and ^{14}C dated by accelerator mass spectrometry (AMS) at Keck Carbon Cycle AMS Facility (University of California, Irvine CA, USA). Radiocarbon dates were reported using Libby's half-life (5568 yr) and corrected for natural fractionation ($\delta^{13}C$ = −25 ‰ PDB). They were calibrated with the CALIB 6.0 online program [*Stuiver et al.*, 2005] using the IntCal09 calibration data set [*Reimer et al.*, 2009].

[15] Radiochronology of more recent sediments was determined by ^{210}Pb and ^{137}Cs dating techniques [*Appleby*, 2001]. Dried samples of 2 to 4 g (0.25 to 1 cm sampling intervals) were homogenized with a pestle and a mortar, and stored in plastic vials. The vials were immediately sealed and left for a period of 20–30 days (6–7 half-lives of the intermediate product [222]Rn) to attain radioactive equilibrium between parent [226]Ra and granddaughter supported [210]Pb. The samples were then analyzed by gamma ray counting with a low background germanium spectrometer (Ortec DSPEC). Dates and sedimentation rates were obtained by the *excess* [210]Pb (i.e., formed in the atmosphere by the decay of [222]Rn), which represents the difference between *total* (measured) and *supported* (from [226]Ra decay) [210]Pb.

4. Results

4.1. General Stratigraphy

[16] All sediment cores show a relatively sharp transition in their general stratigraphic proxies (Figure 2). This marked shift, also observed in other lithostratigraphic data at the macro- and micro-scales (e.g., grain size and XRF, see next sections), was used to determine the boundary between two main sedimentary facies (units):

[17] 1) The bottom sediments (*lower facies*, > 3–6 cm depth) do not show any visible laminations or sedimentary structures and appear dry and sticky. These massive sediments have a dark gray (Munsell color scale = 2.5 Y 4/1) to a lighter gray (2.5 Y 5/1) color. They show a relatively high bulk density (>1.5 g cm^{-3}), represented by low gray values (<1000) on X-radiographs (dark gray to black). Compared to the overlying sediments, they also have much lower water content (20–25%), LOI values (<5%), and ITRAX incoherent on coherent scattering ratios (inc/coh < 3), the latter being partly related to sediment porosity and organic content [*Croudace et al.*, 2006].

[18] 2) The top sediments (*upper facies*, from 3 to 6 cm depth to the surface) are generally finely laminated (≤1 mm) and appear relatively soft and wet. These sediments have a dark grayish brown (2.5 Y 4/2) to a lighter grayish brown (2.5 Y 5/2) color. They show a relatively low bulk density (<1 g cm^{-3}), represented by high gray values (>2000) on X-radiographs (light gray). They also have significantly higher water content (60–80%), LOI values (6–10%), and inc/coh ratios (>3) than the underlying sediments.

[19] The boundary or transition zone between these two sedimentary units generally consists of mm- to cm-scale organic-rich horizons in the form of macroscopic peat/plant debris or as thin millimetric dark grayish brown (2.5 Y 3/2) layers. More detailed physical and chemical descriptions are outlined in the following sections.

4.2. Long-Term and Short-Term Chronology

[20] The lower facies appear considerably older than the upper facies, as shown by radiocarbon dating on discrete samples (Table 2). Calibrated ages span from ~1000 to ~8000 cal yr BP in the bottom sediments and from «modern» to ~500 cal yr BP in the top sediments, suggesting a probable sedimentation gap between the two facies. If continuous sedimentation is assumed during the lower facies deposition, very low accumulation rates (<0.005 cm yr^{-1}) may have controlled the deposition of these sediments. There is an age inversion in one core (K12P2), suggesting that ^{14}C ages (especially from bulk sediments) have to be interpreted cautiously, as discussed in greater detail below (section 5.3).

[21] According to short-lived radioisotope activities (^{210}Pb and ^{137}Cs), only the top sediments (upper facies) can be considered as recent, i.e., less than 150 years-old (Figure 3). For most analyzed cores, equilibrium depth
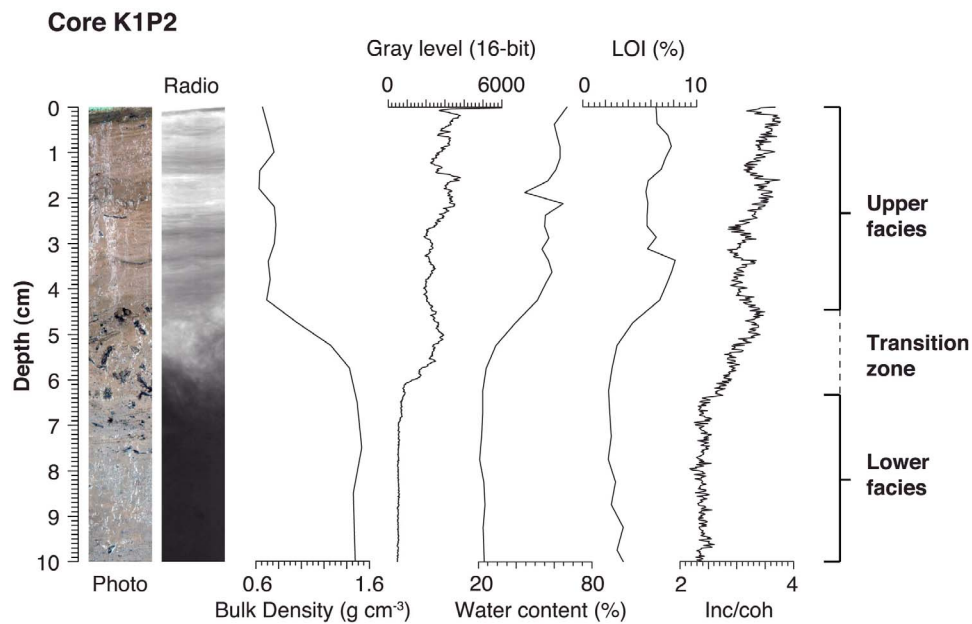
Figure 2. General stratigraphy for core K1P2. From left to right: 500 dpi digital photograph (Photo); 16-bit gray scale micro-radiograph (Radio); dry bulk density, calculated from sediment organic content and wet/dry mass measurements; 16-bit gray level values from the micro-radiograph; sediment water content (%); loss-on-ignition (LOI) after 550°C combustion (4 h); Inc/coh = incoherent on coherent scattering ratio (see section 3 for details).

Table 2. Radiocarbon (^{14}C) and Calibrated (cal yr BP) Ages From Sampled Ponds[a]

Core	Depth (cm)	Lab	Material	Age (^{14}C yr BP)	1σ Range (cal yr BP)	Midpoint (cal yr BP)
K1P2 (t)	4.0–4.5	ULA-1657	bulk sediment	555 ± 15	540–620	580
K1P2 (b)	12.0–12.5	ULA-1658	bulk sediment	1710 ± 15	1570–1690	1630
K2P1 (b)	4.0–4.5	ULA-1648	bulk sediment	1030 ± 15	930–960	945
K2P1 (b)	16.0–16.5	ULA-1649	bulk sediment	7165 ± 25	7960–8000	7980
K2P2 (b)	16.0–16.5	ULA-1682	bulk sediment	6495 ± 20	7340–7430	7385
K6P1 (t)	2.0–2.5	ULA-1650	bulk sediment	140 ± 20	10–270	140
K6P1 (b)	19.5–20.0	ULA-1651	bulk sediment	6225 ± 20	7030–7240	7135
K6P2 (t)	2.0–2.5	ULA-540	plant debris	195 ± 15	150–290	220
K6P2 (t)	3.0–3.5	ULA-1685	bulk sediment	100 ± 20	30–250	140
K12P2 (b)	3.0–3.5	ULA-1689	bulk sediment	1055 ± 20	930–970	950
K12P2 (b)	8.0–8.5	ULA-1690	bulk sediment	6950 ± 20	7740–7820	7780
K12P2 (b)	14.5–15.0	ULA-1691	bulk sediment	3325 ± 15	3480–3580	3530
K16P1 (b)	2.5–3.0	ULA-1692	bulk sediment	2590 ± 20	2730–2750	2740
K16P1 (b)	10.0–10.5	ULA-1693	bulk sediment	2930 ± 15	3010–3150	3080
K16P1 (b)	18.5–19.0	ULA-1694	bulk sediment	3325 ± 15	3480–3580	3530
K16P2 (t)	1.8–2.2	ULA-523	plant debris	modern		
K16P2 (t)	2.5–3.0	ULA-1652	bulk sediment	modern		
K16P2 (b)	17.0–17.5	ULA-1656	bulk sediment	3605 ± 15	3890–3960	3925
K20P1 (t)	2.0–3.0	ULA-1695	bulk sediment	370 ± 15	330–480	405
K20P1 (b)	15.0–16.0	ULA-1696	bulk sediment	825 ± 15	700–740	720

[a]Samples (bulk sediment or organic debris) were extracted from top (t) or bottom (b) sediments (upper and lower facies, respectively). One σ range = 1 standard deviation (68% confidence interval). Radiocarbon (^{14}C) ages were calibrated by the CALIB 6.0 program [*Stuiver et al.*, 2005] using the IntCal09 calibration data set [*Reimer et al.*, 2009].
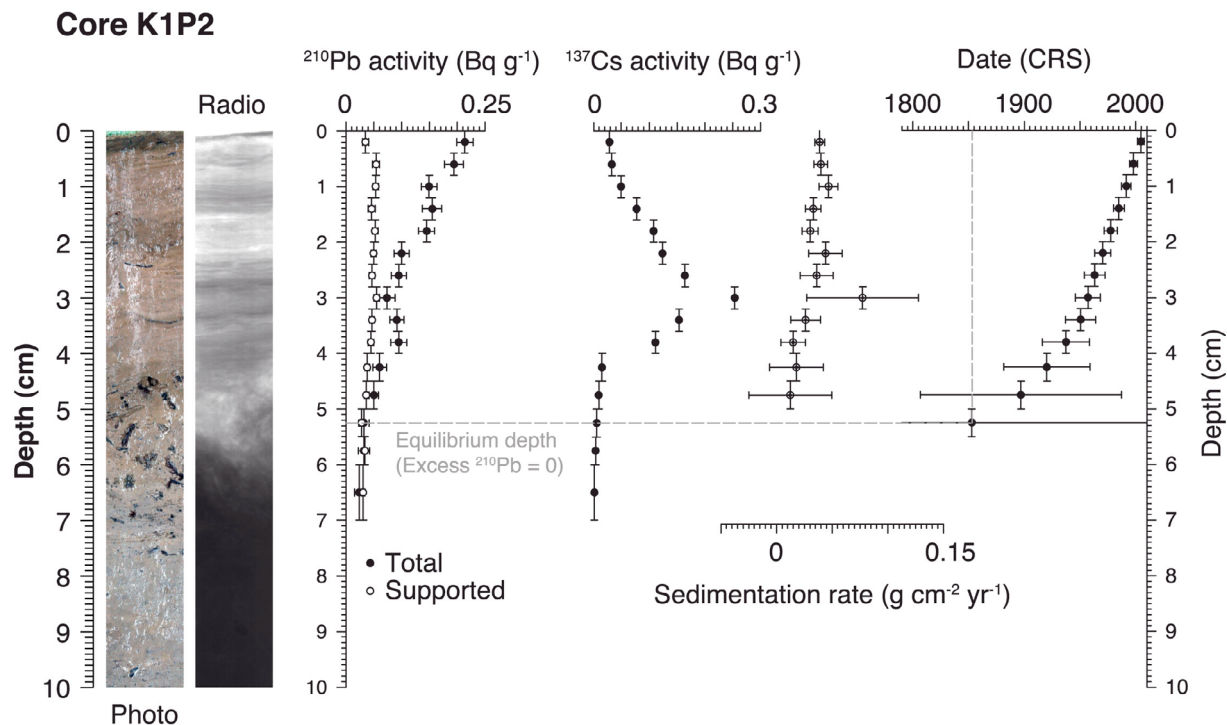
Core K1P2

Figure 3. Recent chronology (^{210}Pb and ^{137}Cs) for core K1P2. From left to right: 500 dpi digital photograph (Photo); 16-bit gray scale micro-radiograph (Radio); total (measured) and supported (from ^{226}Ra decay) ^{210}Pb activity (the difference gives the *excess* ^{210}Pb); ^{137}Cs activity; calculated sedimentation rate (mass accumulation in g cm^{-2} yr^{-1}); constant rate of supply (CRS) chronology model [*Appleby*, 2001]. Vertical (depth) and horizontal (activity, sedimentation rate or date) error bars are shown.

(where excess ^{210}Pb tends to 0) corresponds precisely to the base of this upper unit. Additionally, the ^{137}Cs profile shows a well-defined (i.e., sharp) peak at ~3 cm, indicating that sediment mixing or chemical diffusion in these sediments can be considered as negligible. Since ^{210}Pb activities do not show a perfect logarithmic decrease with depth, the *constant rate of supply* (CRS) model, assuming a constant atmospheric supply in excess ^{210}Pb but taking into account variations in sedimentation rate, has been chosen to date each sampled slice of sediment (mid-section). According to this model, the depth at which ^{137}Cs activities reach a peak (maximum atmospheric fallout from nuclear weapon tests in 1963) corresponds to the highest calculated sedimentation rate, ranging from AD 1955 to AD 1965. Considering measured ^{210}Pb activities and sedimentation rates at different core depths, atmospheric excess ^{210}Pb flux is estimated at 50 to 80 Bq m^{-2} yr^{-1}, a value in the range of published data for several lakes in the northern hemisphere [*Appleby*, 2001].

4.3. Particle Size and Texture

[22] Sediments generally show a polymodal grain size distribution and are poorly to very poorly sorted (sorting values between 3 and 5 [*Blott and Pye*, 2001; *Krumbein and Pettijohn*, 1938]). Downcore surface plots of particle size distribution have been used in combination with conventional statistical parameters (Figure 4). Bottom sediments are mostly distributed in a dominant mode or grain size class (>3% abundance) at 1–10 μm, while secondary modes are observable at 20–40 and 100–200 μm. The comparison of surface plots and statistical profiles reveals that the mean (4–5 μm) and median (3–4 μm) grain sizes are included in the dominant mode (1–10 μm), whereas the standard deviation (sorting) is relatively variable and higher than 4 μm. This facies is mainly composed of silt (~60%), with a notable fraction of clay (~30%) and a minor proportion of sand (<10%, exclusively fine sand = 63–250 μm). Contrastingly, top sediments are distributed in at least 3 significant modes (>2%): 0.2–0.4 μm, 1–2 μm and 4–5 μm. Additional and less significant modes (<1%) can be seen at 8–10 μm and 20–40 μm. The mean and median grain sizes (~1.5 μm both) correspond to the dominant mode (1–2 μm, > 4%), while the sorting is relatively stable at ~3 μm. This facies is dominated by clay particles (~60%), with a major proportion of silt (~40%) and a negligible sand fraction. Considering both facies, mean and median grain sizes are correlated with clay and silt percentages, whereas standard deviation (sorting) profiles coincide with sand percentage in the lower facies, where the distribution is coarsely skewed (mean > median grain size).

[23] At the microscopic scale, the analysis of thin sections revealed contrasting texture and size of particles between sedimentary facies (Figure 5). The lower facies consists mostly of silt/sand angular grains (mainly quartz and feldspath) floating in a fine siliciclastic matrix. Very few organic remains or diatom frustules are observable. In contrast, upper facies appears finely laminated as shown by mm-scale alternation of darker and lighter layers, although the boundaries between those layers are not always visible.
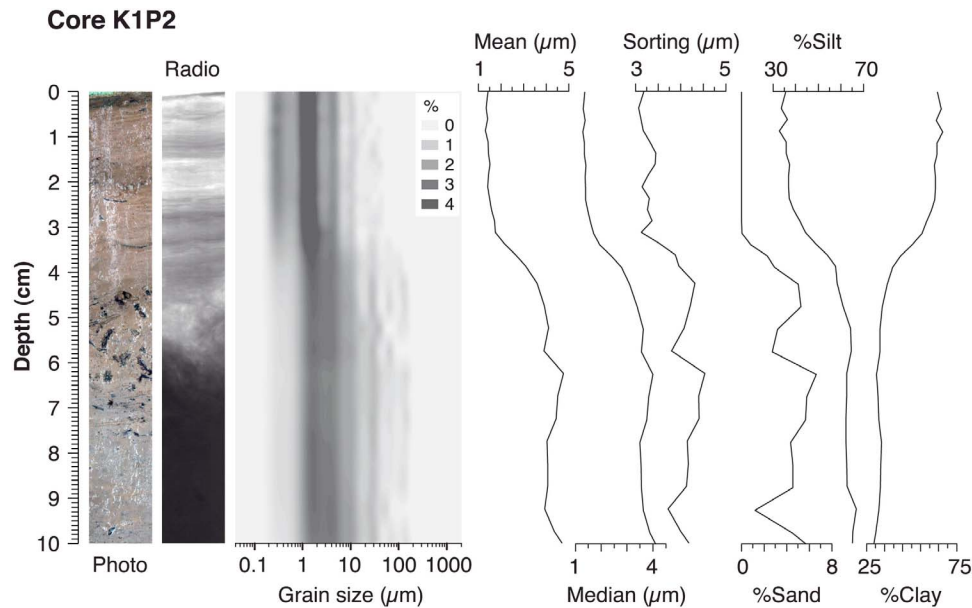
Figure 4. Grain size analysis for core K1P2. From left to right: 500 dpi digital photograph (Photo); 16-bit gray scale micro-radiograph (Radio); grain size 3D surface plots (z axis = volume %); statistical grain-size parameters (mean, median, sorting/standard deviation, sand, silt and clay percentages) calculated by the GRADISTAT 4.0 software using the method of moments [*Blott and Pye*, 2001].

Very fine black spherules (few microns in diameter) and diatom frustules are also identified, especially in the lighter layers. The transition zone between the two facies generally contains organic matter in the form of scattered, matrix-supported peat debris (*Sphagnum* spp. and/or other mosses). These organic-rich horizons vary from a few millimeters to 2–3 cm in thickness.
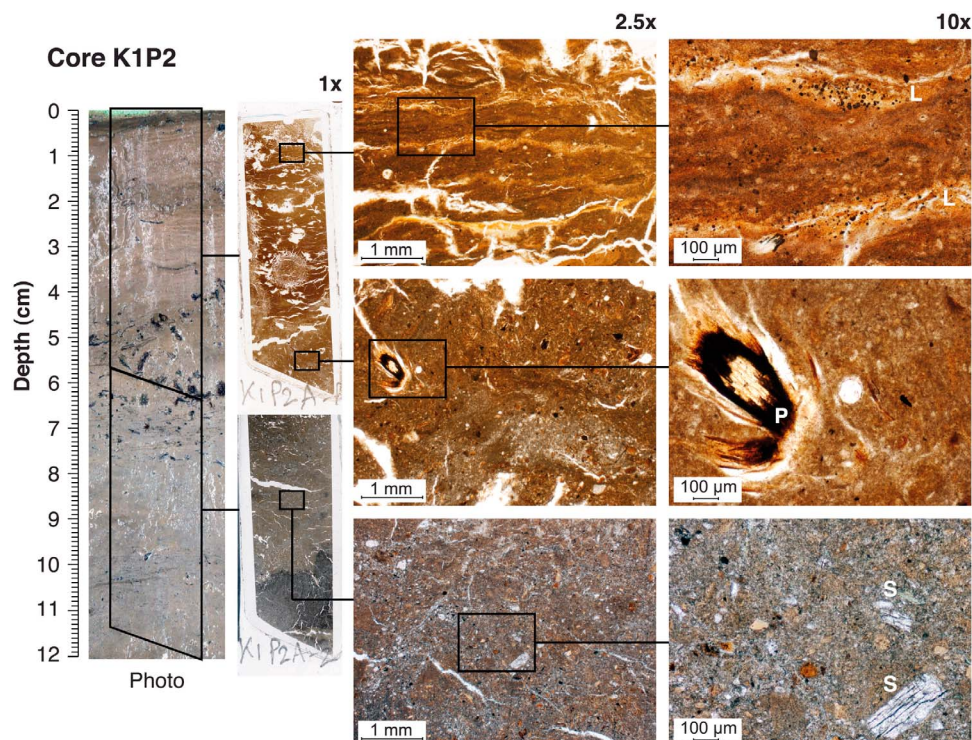

Figure 5. Thin sections of core K1P2. From left to right: 500 dpi digital photograph (Photo); impregnated thin sections (1× scale); plain light images obtained with a petrographic microscope (2.5× and 10× magnification). L = lighter layers; P = peat debris (*Sphagnum* spp.); S = sand grains.

4.4. Geochemistry (XRF)

[24] Sediment cores contain > 20 detectable chemical elements, but many of them show noisy profiles or values near the detection limit of the instrument [*Croudace et al.*, 2006]. Therefore, only the most relevant elements were selected for discussion: K-Ti-Rb-Zr (detritic fraction); Fe-Mn (redox sensitive elements); Ca-Sr (carbonate fraction); and P-S (organic fraction). Some element ratios have also been plotted in order to detect unusual or out-of-range geochemical inputs different from the detritic background (Figure 6a). For almost all selected elements, the overall trend is a general decrease toward the core surface. However, some sharp variations appear mainly at the boundary between the sedimentary facies (~6 cm for core K1P2). Some elements or elemental ratios (e.g., K, Ti, K/Ti, Fe, Ca) show a sudden decrease at those depths, whereas other elements/ratios (e.g., Zr/K, Fe/Ti, Fe/Mn) show marked peaks. Finally, some elements (Mn, P, S) do not show any marked changes.

[25] Geochemical properties of the lower and upper facies can be further analyzed on scatter diagrams of selected elements by plotting mm-averaged XRF data intervals representative of bottom and top sediments, respectively (Figure 6b). Points of the lower facies (8–9 cm) generally plot apart from upper facies clusters (1–2 cm), indicating different geochemical properties. Detritic elements (K, Ti) and carbonate elements (Ca, Sr) show the greatest discrepancies between top and bottom sediments, whereas S and P are much more evenly distributed.

[26] When all study ponds are considered simultaneously (Figure 7), the lower facies (8–9 cm intervals) also separates from the upper facies (1–2 intervals). This trend is more pronounced for both cores of pond K6 (blue-green water color), but less notable for ponds K16 and K20 (beige water color). For almost all elements (except Zr and Sr), pond K6 yields the greatest difference between minimum (top sediments) and maximum (bottom sediments) values. Incoherent versus coherent scattering show a different separation pattern, much less pronounced for sediment type (top versus bottom) than for pond color, i.e., the blue-green pond (K6) plotting clearly apart from the brown pond (K1), with black (K12) and beige ponds (K16 and K20) occupying an intermediate position.

5. Discussion

5.1. Nature/Age of the Lower Facies

[27] The results obtained from the lower facies show that these sediments were deposited in a low organic and low energy environment. Most notable indications are their low amount of organic matter, their clayey silt grain size, the presence of coarser matrix-supported grains (mainly quartz and feldspar), and the absence of sedimentary structures. Compared to the overlying sediments, this facies show much lower inc/coh ratios, a parameter inversely correlated with the atomic mass of the sediment matrix and mainly influenced by matrix density, porosity and organic matter content [*Croudace et al.*, 2006]. Figure 2 shows that gray level values (related to matrix density), water content (related to porosity) and LOI (organic carbon approximation) are indeed well correlated with inc/coh profiles. These

sediments also show very few (minor) changes in XRF profiles or scatterplots (Figure 6), suggesting relatively homogeneous conditions during their deposition. Finally, they contain no or only very few preserved organic remains or diatom frustules.

[28] Considering its geographic location (~20 km inland from Hudson Bay coast) and altitude (~105 m a.s.l.), the study site was affected by the postglacial Tyrrell Sea transgression from local deglaciation ca. 8000 cal yr BP until its post-glacial emergence ca. 6000 cal yr BP [*Arlen-Pouliot and Bhiry*, 2005; *Dyke and Prest*, 1987; *Hillaire-Marcel*, 1976; *Lajeunesse and Allard*, 2003]. This episode must have left thick marine littoral deposits in fluvial valleys that were submerged at that time. Thus, the lower facies represent fine-grained marine sediments deposited during the postglacial Tyrrell Sea episode. Similar deposits, found in nearby locations, could support this interpretation:

[29] 1) The occurrence of marine littoral deposits underlying typical lacustrine sediments in Lake Kachishayoot, located 8 km west of our study site at a similar altitude of 100 m a.s.l. [*Miousse et al.*, 2003; *Saulnier-Talbot and Pienitz*, 2001]. These sediments, attributed to the Tyrrell Sea episode, consist of organic-poor (<5%) silts/clays and littoral sands containing fossil marine coastal diatom taxa (salinity tolerance = 1–35%) and foraminifers. Radiocarbon dates obtained on transitional sediments between marine and lacustrine units yielded a post-glacial emergence of this site and isolation from marine waters between 5400 cal yr BP [*Saulnier-Talbot and Pienitz*, 2001] and 6200 cal yr BP [*Miousse et al.*, 2003].

[30] 2) Silt and clay marine sediments found under thick peat deposits in two different palsa fields near Kuujjuarapik-Whapmagoostui, at comparable altitudes of 110 and 95 m a.s.l., respectively [*Arlen-Pouliot and Bhiry*, 2005; *Bhiry and Robert*, 2006]. The basal peat layers yielded an estimated emergence age of 5800 cal yr BP at 110 m a.s.l. [*Arlen-Pouliot and Bhiry*, 2005] and 4600 cal yr BP at 95 m a.s.l. [*Bhiry and Robert*, 2006].

[31] 3) The presence of glacio-marine fine-grained sediments in mineral permafrost mounds (lithalsas) on the eastern coast of Hudson Bay near Umiujaq (56°37′ N; 76°13′ W) at 185 m a.s.l. [*Calmels et al.*, 2008]. No radiocarbon dates could be obtained due to a lack of datable material, but these fine sediments have also been attributed to the Tyrrell Sea transgression and are massive and organic-poor (mean LOI = 1%), like the sediments described above.

[32] This interpretation is further supported by radiocarbon dates older than 6000 cal yr BP (ranging from ~7000 to ~8000 cal yr BP) obtained inside this massive unit (Table 2). However, some other samples taken in that unit have provided much younger dates (ranging from ~2000 to ~4000 cal yr BP, see section 5.3 below).

[33] Nevertheless, the absence of marine faunal (e.g., foraminifers) and floral (e.g., diatoms) fossils in these sediments is striking. A similar scenario has been reported from postglacial deposits along the southeastern [*Hillaire-Marcel*, 1976] and eastern [*Lajeunesse*, 2008] coasts of Hudson Bay, some even showing negligible pore water salinity [*Calmels et al.*, 2008]. Two potential and mutually non-exclusive explanations were proposed: 1) very cold and turbid freshwaters originating from retreating inland ice masses (ca. 6000 cal yr BP), preventing the development of
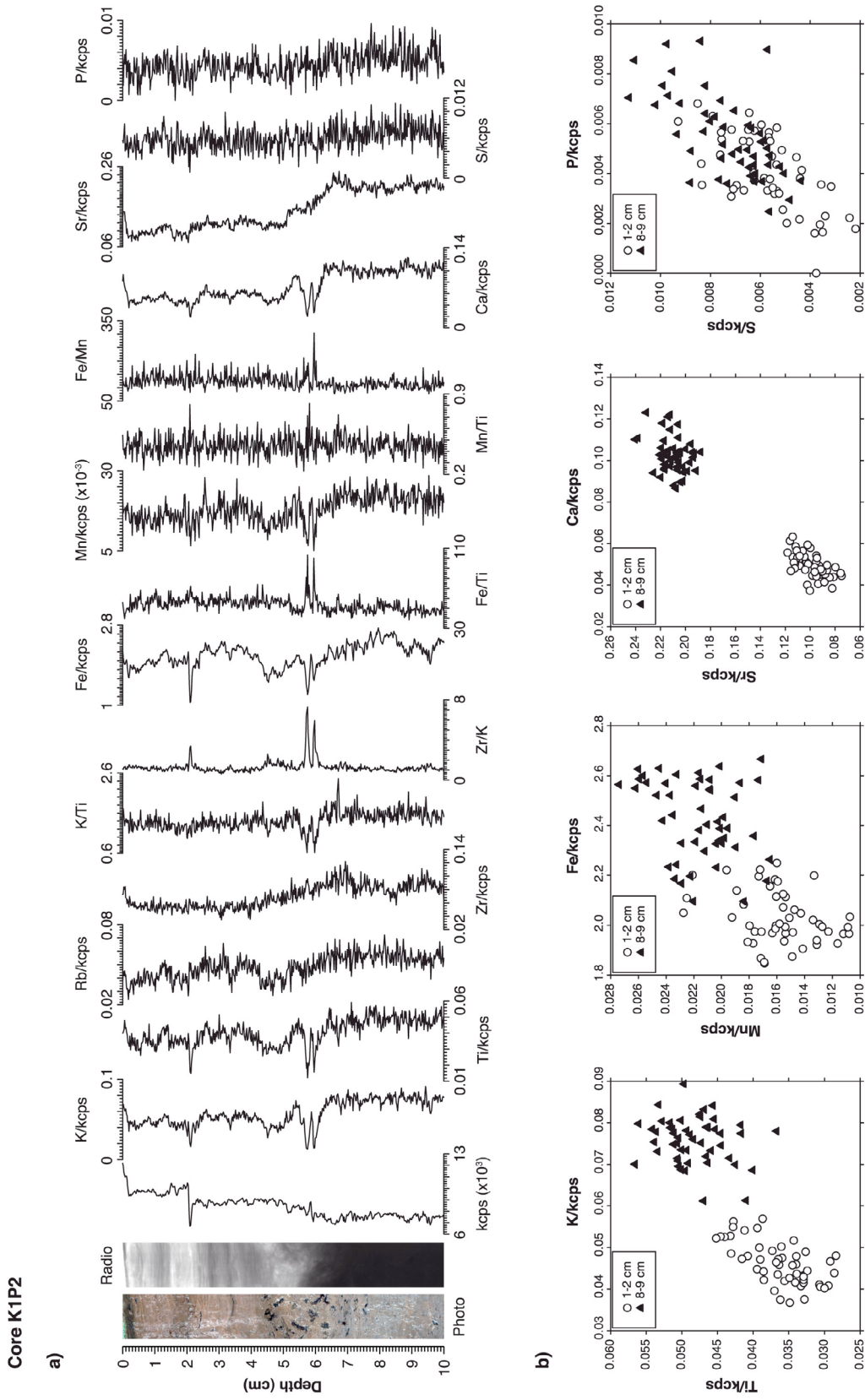
Figure 6. X-ray fluorescence (XRF) data for core K1P2. (a) Vertical profiles along the core. (b) Scatterplots of selected elements. Results are given in peak area integrals normalized by the total counts per second of each spectrum (kcps = 10^3 counts per second).
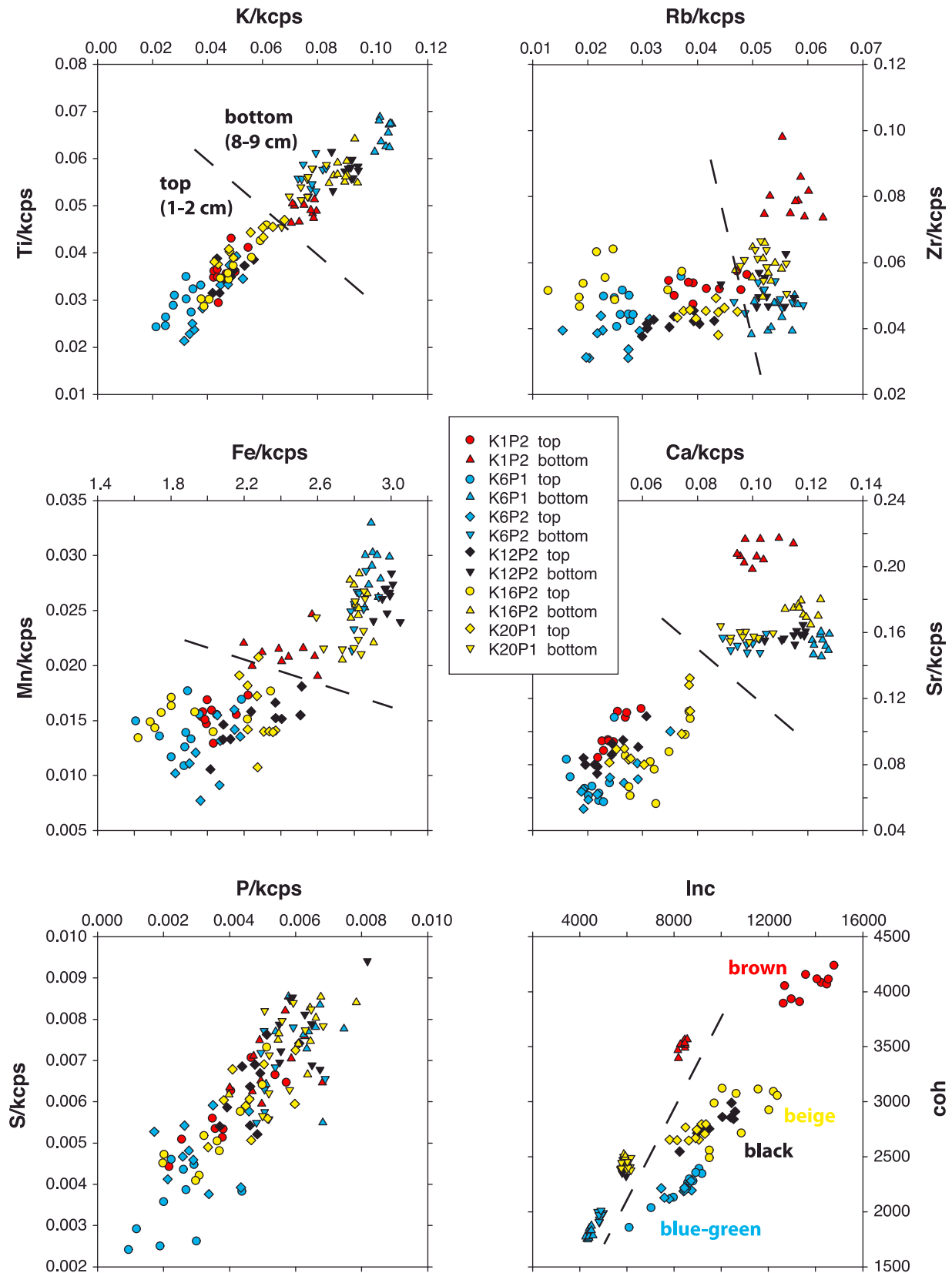
Figure 7. XRF scatterplots of selected elements for all sampled ponds. Results are given in peak area integrals normalized by the total counts per second of each spectrum (kcps = 10^3 counts per second). Inc and coh = incoherent and coherent scattering values, respectively.

aquatic biota in shallow coastal waters; and 2) complete salt leaching of these sediments between their postglacial emergence ca. 6000 cal yr BP and permafrost inception, not until 3200 cal yr BP at northern sites and around 1500 cal yr BP at southern sites [*Calmels et al.*, 2008].

5.2. Nature/Age of the Upper Facies

[34] The results obtained from the upper facies show that these sediments were deposited as lacustrine organic-rich and humic muds (gyttja). Most notable features are their low density, their high organic matter content, the silty clay grain size, and the scarcity of sand grains. Compared to the underlying facies, these sediments have much higher inc/coh ratios, gray level values, water content and LOI (Figure 2). This enhancement in organic matter content is consistent with recent limnological surveys in subarctic Quebec indicating high productivity and high concentrations of DOM in these thermokarst ponds [*Breton et al.*, 2009].

[35] Top sediments also have relatively low chemical element concentrations (as inferred from XRF values) compared with the underlying facies. This general trend is observable for almost all analyzed elements (vertical profiles or scatterplots). Considering sufficiently constant geochemical inputs from the catchment and surroundings (by weathering, surface runoff, wind erosion, etc.) during the lacustrine phase, this relative impoverishment in major chemical elements could be due to the partial recycling of pond waters resulting from the sharp decrease in leaching of glacial/marine sediments in the surroundings, formerly exposed to surface erosion but more recently covered (protected) by the development of peatland vegetation and soils. The application of a diatom-based lake alkalinity model on the microfossil assemblages from a sediment core of Lake Kachishayoot, 8 km west of our study site [*Saulnier-Talbot and Pienitz*, 2001], has documented a significant decrease in lake water alkalinity (inorganic elements and major ions) and simultaneous increase in DOC concentrations following the mid-Holocene isolation of the lake from post-glacial Tyrrell Seawaters and subsequent terrestrial vegetation re-colonization in its catchment.

[36] In most analyzed cores, the base of the upper facies (i.e., the sharp transition zone between top and bottom sediments) contains relatively high amounts of organic matter, both at macroscopic (visible peat and plant debris) and microscopic scales (*Sphagnum* spp. and/or other moss taxa on thin sections). This organic layer is always positioned directly above the marine sediments and was not observed elsewhere in analyzed cores, excluding the occurrence of multiple pond-palsa-pond cycles as described in other thermokarst systems [*Zoltai*, 1993]. Considering that thawing of permafrost mounds (either organic or mineral), accompanied by local subsidence, was the main cause driving subarctic thermokarst pond inception, these organic-rich horizons may represent ancient palsa/lithalsa summits that were partially eroded and subsequently submerged [*Calmels et al.*, 2008]. It is therefore possible that the variable extent of peat patches remaining at pond inception is partly driving contemporary concentrations of DOM in these relatively productive aquatic systems, with apparently very small drainage basin (mostly limited by the peripheral ridge), long water renewal time, and continuously strong allochthonous signal [*Breton et al.*, 2009]. Moreover, these peat patches overlying the silt/clay layer are possibly influencing the degree of inorganic particle resuspension in the water column, thus the TSS content. DOM and TSS contents have been shown to largely control the optical properties [*Watanabe et al.*, 2011], the temperature and oxygen profiles, the degree of heterotrophy, and thus the production of GHG [*Laurion et al.*, 2010].

[37] On XRF profiles (Figure 6a), elements or element ratios generally associated with fine detritic inputs (e.g., K, K/Ti) show a sudden decrease at those depths, whereas elements or ratios reflecting authigenic precipitation of redox-sensitive minerals (e.g., Fe/Ti, Fe/Mn) show marked peaks. These results indicate enhanced precipitation of neoformed minerals in well-oxygenated conditions (redox limit in/near the sediment interstitial water) at the beginning of pond inception, i.e., in years following permafrost mound thaw and subsidence. Such peaks in redox-sensitive elements are rarely observed elsewhere in the upper facies, suggesting that anoxic/hypoxic conditions (at least seasonally, i.e., during persistent thermal stratification episodes) gradually developed in bottom waters, as the redox limit migrated upward in the water column. These anoxic/hypoxic conditions are a prominent feature of these thermokarst ponds that show thermal stratification for most part of the year and very short or absent spring mixing period [*Breton et al.*, 2009; *Laurion et al.*, 2010; unpublished data, 2011].

[38] Another notable feature at the boundary between lower and upper facies is the significant drop in Ca and Sr values (Figure 6a). This suggests a low-pH (acidic) environment at that moment, consistent with the presence of peatland vegetation/soils in the surroundings. Presently, all ponds except one have pH values < 7 (Table 1). Similar water conditions (circumneutral to acidic), mainly resulting from enhanced fulvic/humic acid inputs from the catchment basin, have also been observed in nearby Lake Kachishayoot [*Saulnier-Talbot et al.*, 2003].

[39] Radiocarbon dates obtained within the base of the upper facies ranged from 300 to 400 cal yr BP to less than 1000 cal yr BP (Table 2). These ages must be considered as *maximal* (i.e., oldest) ages, since younger organic material may have been eroded from the summit of palsa/lithalsa before their collapse. Despite these uncertainties, our results generally agree with other studies concerning permafrost development in palsa fields near this study site, starting ca. 1500 cal yr BP and ending ca. 400 cal yr BP [*Arlen-Pouliot and Bhiry*, 2005; *Bhiry and Robert*, 2006]. In addition, short-term chronological data (^{210}Pb and ^{137}Cs) show that most of the upper sediments were deposited less than 150 years ago (Figure 3). Local thermokarst ponds therefore may have begun to form since the end of the Little Ice Age (i.e., 200–300 years ago).

5.3. Chronological Challenges

[40] The two sedimentary units described above show a significant age difference that may be explained by the long-term evolution of the climatic, hydrologic and geomorphologic conditions in the area. The sediments of the upper facies, deposited since pond inception, yielded some young radiocarbon dates (past centuries) with significant associated errors, often representing more than 10% of the reported age for samples younger than 200 years (Table 2). The ^{14}C dating technique is indeed of limited usefulness for the last

few hundred years [*Björck and Wohlfarth*, 2001]. The $^{210}Pb/^{137}Cs$ dating technique is a valuable alternative for sediments younger than 150 years, most often not exceeding 100 years [*Appleby*, 2001]. Therefore, sediment layers deposited about 100 to 200–300 years ago occupy a temporal range at a «technological void», being too old for the ^{210}Pb dating technique but too young for the ^{14}C technique. In this study, the best approximation was achieved by 1) obtaining ^{210}Pb dates on sediments from maximum core depths (3–5 cm), assuming no or negligible bioturbation (supported by clear ^{137}Cs peaks and the presence of laminations), and 2) dating the organic/peat layers in the basal part of the upper facies, assuming that these ^{14}C dates represent the oldest ages for palsa/lithalsa collapse (i.e., thermokarst pond inception).

[41] Despite careful pre-treatments before radiocarbon measurements, several factors may have influenced the resulting ages, especially when dealing with bulk sediment samples. As the study ponds are surrounded by dense shrub/tree vegetation and are possibly influenced by remains of peat patches, the allochthonous organic fraction of contrasting ages may represent a substantial proportion of the total organic matter in ponds. Therefore, contamination by *older* carbon is likely to have influenced radiocarbon ages in the upper facies. In contrast, contamination by *younger* carbon (e.g., root penetration, percolation of humic acids, downward movement of sediment particles by bioturbation) cannot be ruled out with respect to the lower facies, at least in samples from near its boundary with the overlying sediments. Younger than suspected ages (<6000 cal yr BP) were obtained in that facies (Table 2), and these potential errors may be due to contamination by either rootlets or humic acids from the overlying peat deposits, as documented in other studies [*Björck and Wohlfarth*, 2001]. Moreover, establishing a reliable chronology for those sediments is quite limited by the lack of datable material, a situation documented elsewhere around Hudson Bay at comparable altitudes [*Calmels et al.*, 2008; *Hillaire-Marcel*, 1976; *Lajeunesse*, 2008].

[42] Considering all the aforementioned challenges, the established chronology must be interpreted with caution within the context of the dynamic development of permafrost mounds. Many processes have the potential to remove or displace sediments, contributing to a disturbance of radiocarbon sources. The peat cover of mature palsas is likely to be desiccated and degraded along polygonal extension cracks, delineating peat blocks that can slide toward the edges and eventually disintegrate. Organic or mineral top layers can also be eroded by winds, drifting snow/ice crystals or rain [*Seppälä*, 1986]. Once the peat cover is completely eroded, frostboiling (convection in the fine-grained active layer under freeze-thaw cycles) can disturb fine-grained layers, slowly carrying surface soil from a lithalsa's summit toward its periphery [*Calmels et al.*, 2008]. Finally, freezing in the core of a palsa/lithalsa leads to cryo-desiccation and consolidation of the silt/clay layers between ice lenses, which may cause internal sediment disturbance [*Konrad and Seto*, 1994]. The final result is a stratigraphic discontinuity affecting the highly frost-susceptible layers in the lower facies.

5.4. Variability in Pond Color

[43] XRF scatterplots of incoherent versus coherent scattering show a notable contrast between ponds that appears to be related to their apparent water color (i.e., black, blue-green, brown or beige; Figure 7). The inc/coh scattering being partly controlled by sediment organic matter content [*Croudace et al.*, 2006], it could possibly reflect past pond water color. Diatom-inferred estimates of past DOC concentrations and water color from subarctic lake sediments [*Saulnier-Talbot et al.*, 2003] revealed a strong relationship between these two components since lake isolation from postglacial marine influence during the mid-Holocene. However, organic matter content alone cannot entirely explain the observed differences in pond colors or inc/coh values in sediments, because sediment matrix properties (e.g., mineralogy, density, porosity) also control inc/coh values [*Croudace et al.*, 2006]. Hence, the contrasting results obtained for ponds of different color (Figure 7) could also be related to differing concentrations of inorganic matter. Recent analysis of the optical properties of these ponds [*Watanabe et al.*, 2011] showed that color differences can mostly be attributed to varying concentrations of two optically active substances, namely DOM (expressed as DOC; responsible for spectral absorption) and suspended non-algal particulate matter (approximated by TSS; contributing to spectral scattering and absorption). In the latter case, high concentrations of fine particles (silts and clays) in thermokarst ponds are likely to have a large impact on water color.

[44] The optical properties of thermokarst ponds have likely changed in the recent past, depending on sediment settling in the water column and vegetation development in their catchment. The CRS ^{210}Pb models (Figure 3) suggest that sedimentation rates in some of the study ponds have been higher in the middle of the 20th century (mainly 1950s and 1960s), which coincides with increases in annual precipitation and permafrost thawing across the southeastern Hudson Bay region [*Payette et al.*, 2004]. Since that time, sedimentation rates appear to have gradually decreased, possibly due to the settling of clay and silt particles (decreasing TSS) and the stabilization of shores by terrestrial/aquatic vegetation development (increasing DOC/DOM), resulting in a transition from turbid green or beige to dark brown or yellowish black color. However, the potential influence of peat patches present during pond inception may interfere with this trend by partly controlling contemporary concentrations of DOM and silt/clay particles (see section 5.2 above). On the other hand, sedimentation rates do not appear to have recently decreased in several other ponds that provided very young ages within a thinner upper facies (e.g., K16 – turbid beige color; Figure S1).[1] This observation suggests a possible link between the turbidity and age of ponds, i.e., more turbid beige ponds (high TSS) being younger than less turbid brown/black ponds (low TSS). Tables 1 and 2 show that pond K16 has indeed the highest turbidity (TSS > 24 mg L^{-1}) and the thinnest upper facies (<2 cm) of the studied ponds, and also provided the youngest ^{14}C dates (*modern*, i.e., post-1950). More short-term chronologies in a larger series of thermokarst ponds and detailed

---

[1]Auxiliary materials are available with the HTML. doi:10.1029/2011JG001675.

paleolimnological reconstructions (e.g., diatom-based inferences of water color and DOC) are necessary to confirm and quantify these inferred relationships.

[45] As optically active substances closely linked to water color (DOC, TSS) can influence GHG production in aquatic systems [*Laurion et al.*, 2010; *Sobek et al.*, 2003], that type of chronologies and relationships should help to elucidate temporal changes in GHG emissions. To fully appreciate the natural variability and past limnological dynamics of this type of thermokarst ponds, forthcoming research will focus on two additional aspects: 1) biostratigraphic data (analysis of fossil diatoms) to complement the lithostratigraphic data discussed above by inferring paleolimnological conditions that have major impacts on GHG emissions and carbon cycling (e.g., DOM, water transparency, thermal structure and alkalinity); 2) recent pond sedimentation dynamics (e.g., sediment trap data) to identify links between their hydrological/geomorphological, limnological and sedimentological properties.

6. Summary and Conclusions

[46] Despite strikingly different water color and limnological conditions, the studied thermokarst ponds showed comparable sedimentological and geochemical properties. The sediment cores consisted of fine organic-rich lacustrine muds overlying organic-poor postglacial marine silts and clays. XRF-inferred concentrations of most chemical elements were similar between ponds and showed decreasing trends from bottom to surface sediments, suggesting a progressive decrease in water alkalinity associated with the stabilization of soils in the surrounding catchments. The optical diversity of thermokarst ponds related to varying combinations of optically active substances (DOC and TSS) is therefore more likely linked to conditions during and following pond inception (e.g., peat patches and soil stabilization by vegetation development) rather than to long-term general chemical composition.

[47] The results of our lithostratigraphic analyses generally agree with palsa/lithalsa developmental stages as observed in discontinuous permafrost landscapes: 1) permafrost inception and development (~1500 to 400 cal yr BP in the southern discontinuous zone in subarctic Quebec) in fine and frost-susceptible sediments (peat and/or clay); 2) permafrost erosion, thaw and subsidence, resulting in the formation of shallow, water-filled topographic depressions; 3) pond evolution through the development of seasonal thermal stratification in the water column and anoxic/hypoxic conditions in the bottom waters.

[48] Recent degradation of permafrost in arctic/subarctic regions is considerably modifying the global carbon pool by means of feedback mechanisms involving climate, water balance and biogeochemical cycles [*Laurion et al.*, 2010; *Schuur et al.*, 2008; *Walter et al.*, 2007]. Thermokarst lakes and ponds, with their highly organic waters and catchments, are expected to play a major role in future climate dynamics, but the controlling processes have yet to be quantified at different temporal and spatial scales. In this regard, sedimentological studies (such as presented here) that explore the variability and temporal evolution of thermokarst ponds, can serve to identify and interpret the biogeological processes involved. Among major factors affecting organic

matter properties in subarctic thaw ponds, their development stage (age) is likely to control their trophic state and stability (e.g., through microbial community composition, aquatic plant/peat colonization, reduced erosion/suspension of clay particles) [*Breton et al.*, 2009]. Thus, the temporal dynamics of thermokarst ponds should have a significant impact on the intensity and direction of future carbon fluxes.

References

Allard, M., and M. K. Seguin (1987), Le pergélisol au Québec nordique: Bilan et perspectives, *Geogr. Phys. Quat.*, 41(1), 141–152.

Allard, M., and G. Tremblay (1983), La dynamique littorale des îles Manitounuk durant l'Holocène, *Z. Geomorphol.*, 47, 61–95.

Appleby, P. G. (2001), Chronostratigraphic techniques in recent sediments, in *Tracking Environmental Change Using Lake Sediments*, vol. 1, *Basin Analysis, Coring, and Chronological Techniques*, edited by W. M. Last and J. P. Smol, pp. 171–203, Springer, Dordrecht, Netherlands.

Arlen-Pouliot, Y., and N. Bhiry (2005), Palaeoecology of a palsa and a filled thermokarst pond in a permafrost peatland, subarctic Quebec, Canada, *Holocene*, 15(3), 408–419, doi:10.1191/0959683605hl818rp.

Barber, D. C., et al. (1999), Forcing of the cold event of 8,200 years ago by catastrophic drainage of Laurentide lakes, *Nature*, 400(6742), 344–348, doi:10.1038/22504.

Beierle, B. D., S. F. Lamoureux, J. M. H. Cockburn, and I. Spooner (2002), A new method for visualizing sediment particle size distributions, *J. Paleolimnol.*, 27(2), 279–283, doi:10.1023/A:1014209120642.

Bhiry, N., and E. C. Robert (2006), Reconstruction of changes in vegetation and trophic conditions of a palsa in a permafrost peatland, subarctic Québec, Canada, *Ecoscience*, 13(1), 56–65, doi:10.2980/1195-6860(2006)13[56:ROCIVA]2.0.CO;2.

Björck, S., and B. Wohlfarth (2001), 14C chronostratigraphic techniques in paleolimnology, in *Tracking Environmental Change Using Lake Sediments*, vol. 1, *Basin Analysis, Coring, and Chronological Techniques*, edited by W. M. Last and J. P. Smol, pp. 205–245, Springer, Dordrecht, Netherlands.

Blott, S. J., and K. Pye (2001), GRADISTAT: A grain size distribution and statistics package for the analysis of unconsolidated sediments, *Earth Surf. Process. Landforms*, 26(11), 1237–1248, doi:10.1002/esp.261.

Breton, J., C. Vallières, and I. Laurion (2009), Limnological properties of permafrost thaw ponds in northeastern Canada, *Can. J. Fish. Aquat. Sci.*, 66(10), 1635–1648, doi:10.1139/F09-108.

Brown, J., O. J. Ferrians, J. A. Heginbottom, and E. S. Melnikov (1998), Circum-Arctic map of permafrost and ground-ice conditions, Natl. Snow and Ice Data Cent., World Data Cent. for Glaciol., Boulder, Colo.

Calmels, F., M. Allard, and G. Delisle (2008), Development and decay of a lithalsa in northern Quebec: A geomorphological history, *Geomorphology*, 97(3–4), 287–299, doi:10.1016/j.geomorph.2007.08.013.

Croudace, I. W., A. Rindby, and R. G. Rothwell (2006), ITRAX: Description and evaluation of a new multi-function X-ray core scanner, *Geol. Soc. London Spec. Publ.*, 267(1), 51–63, doi:10.1144/GSL. SP.2006.267.01.04.

Dyke, A. S., and V. K. Prest (1987), Late Wisconsinan and Holocene history of the Laurentide ice sheet, *Geogr. Phys. Quat.*, 41(2), 237–263.

Environment Canada (2010), Canadian climate normals or averages 1971–2000, http://climate.weatheroffice.gc.ca/climate_normals/index_e.html, last access 2011–06–01, Natl. Clim. Data and Inf. Arch., Environ. Canada, Fredericton, N. B., Canada.

Francus, P., and C. A. Asikainen (2001), Sub-sampling unconsolidated sediments: A solution for the preparation of undisturbed thin-sections from clay-rich sediments, *J. Paleolimnol.*, 26(3), 323–326, doi:10.1023/A:1017572602692.

Heiri, O., A. F. Lotter, and G. Lemcke (2001), Loss on ignition as a method for estimating organic and carbonate content in sediments: Reproducibility and comparability of results, *J. Paleolimnol.*, 25(1), 101–110, doi:10.1023/A:1008119611481.

Hillaire-Marcel, C. (1976), La déglaciation et le relèvement isostatique sur la côte est de la baie d'Hudson, *Cah. Geogr. Que.*, 20(50), 185–220.

Hillaire-Marcel, C., S. Occhietti, and J.-S. Vincent (1981), Sakami moraine, Quebec: A 500-km-long moraine without climatic control, *Geology*, 9(5), 210–214, doi:10.1130/0091-7613(1981)9<210:SMQAKM>2.0.CO;2.

Konrad, J. M., and J. T. C. Seto (1994), Frost heave characteristics of undisturbed sensitive Champlain Sea clay, *Can. Geotech. J.*, 31(2), 285–298, doi:10.1139/t94-033.

Krumbein, W. C., and F. J. Pettijohn (1938), *Manual of Sedimentary Petrography*, 549 pp., Appleton-Century-Crofts, New York.

Lajeunesse, P. (2008), Early Holocene deglaciation of the eastern coast of Hudson Bay, *Geomorphology*, 99(1–4), 341–352, doi:10.1016/j.geomorph.2007.11.012.

Lajeunesse, P., and M. Allard (2003), The Nastapoka drift belt, eastern Hudson Bay: Implications of a stillstand of the Quebec-Labrador ice margin in the Tyrrell Sea at 8 ka BP, *Can. J. Earth Sci.* 40(1), 65–76, doi:10.1139/e02-085.

Lajeunesse, P., and G. St-Onge (2008), The subglacial origin of the lake Agassiz-Ojibway final outburst flood, *Nat. Geosci.*, 1(3), 184–188, doi:10.1038/ngeo130.

Lamoureux, S. F. (1994), Embedding unfrozen lake sediments for thin section preparation, *J. Paleolimnol.*, 10(2), 141–146, doi:10.1007/BF00682510.

Laurion, I., W. F. Vincent, S. MacIntyre, L. Retamal, C. Dupont, P. Francus, and R. Pienitz (2010), Variability in greenhouse gas emissions from permafrost thaw ponds, *Limnol. Oceanogr.*, 55(1), 115–133, doi:10.4319/lo.2010.55.1.0115.

Lotter, A. F., and G. Lemcke (1999), Methods for preparing and counting biochemical varves, *Boreas*, 28(2), 243–252, doi:10.1111/j.1502-3885.1999.tb00218.x.

Miousse, L., N. Bhiry, and M. Lavoie (2003), Isolation and water-level fluctuations of Lake Kachishayoot, northern Quebec, Canada, *Quat. Res.*, 60(2), 149–161, doi:10.1016/S0033-5894(03)00094-2.

Payette, S., A. Delwaide, M. Caccianiga, and M. Beauchemin (2004), Accelerated thawing of subarctic peatland permafrost over the last 50 years, *Geophys. Res. Lett.*, 31, L18208, doi:10.1029/2004GL020358.

Pienitz, R., P. T. Doran, and S. F. Lamoureux (2008), Origin and geomorphology of lakes in the polar regions, in *Polar Lakes and Rivers: Limnology of Arctic and Antarctic Aquatic Ecosystems*, edited by W. F. Vincent and J. Laybourn-Parry, pp. 25–41, Oxford Univ. Press, Oxford, U. K.

Reimer, P. J., et al. (2009), IntCal09 and Marine09 radiocarbon age calibration curves, 0–50,000 years cal BP, *Radiocarbon*, 51(4), 1111–1150.

Rothwell, R. G., B. Hoogakker, J. Thomson, I. W. Croudace, and M. Frenz (2006), Turbidite emplacement on the southern Balearic Abyssal Plain (western Mediterranean Sea) during Marine Isotope Stages 1–3: An application of ITRAX XRF scanning of sediment cores to lithostratigraphic analysis, *Geol. Soc. London Spec. Publ.*, 267(1), 79–98, doi:10.1144/GSL.SP.2006.267.01.06.

Saulnier-Talbot, E., and R. Pienitz (2001), Postglacial isolation of a coastal basin near Kuujjuaraapik-Whapmagoostui, Hudsonie: A diatom biostratigraphical investigation, *Geogr. Phys. Quat.*, 55(1), 63–74.

Saulnier-Talbot, E., R. Pienitz, and W. F. Vincent (2003), Holocene lake succession and palaeo-optics of a subarctic lake, northern Quebec, Canada, *Holocene*, 13(4), 517–526, doi:10.1191/0959683603hl641rp.

Schuur, E. A. G., et al. (2008), Vulnerability of permafrost carbon to climate change: Implications for the global carbon cycle, *BioScience*, 58(8), 701–714, doi:10.1641/B580807.

Schuur, E. A. G., J. G. Vogel, K. G. Crummer, H. Lee, J. O. Sickman, and T. E. Osterkamp (2009), The effect of permafrost thaw on old carbon release and net carbon exchange from tundra, *Nature*, 459(7246), 556–559, doi:10.1038/nature08031.

Seppälä, M. (1986), The origin of Palsas, *Geogr. Ann. Ser. A*, 68(3), 141–147, doi:10.2307/521453.

Sobek, S., G. Algesten, A. K. Bergstrom, M. Jansson, and L. J. Tranvik (2003), The catchment and climate regulation of pCO$_2$ in boreal lakes, *Global Change Biol.*, 9(4), 630–641, doi:10.1046/j.1365-2486.2003.00619.x.

Stuiver, M., P. J. Reimer, and R. W. Reimer (2005), CALIB 6.0, http://calib.qub.ac.uk/calib/, last access 2011–06–01.

Tarnocai, C., J. G. Canadell, E. A. G. Schuur, P. Kuhry, G. Mazhitova, and S. Zimov (2009), Soil organic carbon pools in the northern circumpolar permafrost region, *Global Biogeochem. Cycles*, 23, GB2023, doi:10.1029/2008GB003327.

Vallee, S., and S. Payette (2007), Collapse of permafrost mounds along a subarctic river over the last 100 years (northern Quebec), *Geomorphology*, 90(1–2), 162–170, doi:10.1016/j.geomorph.2007.01.019.

Veillette, J. J. (1994), Evolution and paleohydrology of glacial Lakes Barlow and Ojibway, *Quat. Sci. Rev.*, 13(9–10), 945–971, doi:10.1016/0277-3791(94)90010-8.

Walter, K. M., S. A. Zimov, J. P. Chanton, D. Verbyla, and F. S. Chapin (2006), Methane bubbling from Siberian thaw lakes as a positive feedback to climate warming, *Nature*, 443(7107), 71–75, doi:10.1038/nature05040.

Walter, K. M., M. E. Edwards, G. Grosse, S. A. Zimov, and F. S. Chapin (2007), Thermokarst lakes as a source of atmospheric CH4 during the last deglaciation, *Science*, 318(5850), 633–636, doi:10.1126/science.1142924.

Watanabe, S., I. Laurion, R. Pienitz, K. Chokmani, and W. F. Vincent (2011), Optical diversity of thaw ponds in discontinuous permafrost: A model system for water color analysis, *J. Geophys. Res.*, G02003, doi:10.1029/2010JG001380.

Zimov, S. A., E. A. G. Schuur, and F. S. Chapin III (2006), Permafrost and the global carbon budget, *Science*, 312(5780), 1612–1613, doi:10.1126/science.1128908.

Zoltai, S. C. (1993), Cyclic development of permafrost in the peatlands of northwestern Alberta, Canada, *Arct. Alpine Res.*, 25(3), 240–246.

F. Bouchard, P. Francus, and I. Laurion, CEN, Université Laval, Pavillon Abitibi-Price, 2405 de la Terrasse, Quebec, QC G1V 0A6 Canada. (frederic.bouchard@ete.inrs.ca)

R. Pienitz, Département de Géographie, Université Laval, Pavillon Abitibi-Price, 2405 de la Terrasse, Quebec, QC G1V 0A6 Canada.